On the Elastic Properties and Fracture Patterns of MoX$_2$ (X = S, Se, Te) Membranes: A Reactive Molecular Dynamics Study

Marcelo Lopes Pereira Júnior [1] , **Cícera Maria Viana de Araújo** [1], **José Moreira De Sousa** [2] , **Rafael Timóteo de Sousa Júnior** [3] , **Luiz Fernando Roncaratti Júnior** [1] , **William Ferreira Giozza** [3] **and Luiz Antonio Ribeiro Júnior** [1,*]

[1] Institute of Physics, University of Brasília, Brasília 70910-900, Brazil; marcelolpjunior@gmail.com (M.L.P.J.); ciceravianafis@gmail.com (C.M.V.d.A.); roncaratti@fis.unb.br (L.F.R.J.)

[2] Federal Institute of Education, Science and Technology of Piauí, São Raimundo Nonato, Piauí 64770-000, Brazil; josemoreiradesousa@ifpi.edu.br

[3] Department of Electrical Engineering, University of Brasília, Brasília 70919-970, Brazil; desousa@unb.br (R.T.d.S.J.); giozza@unb.br (W.F.G.)

* Correspondence: ribeirojr@unb.br

Abstract: We carried out fully-atomistic reactive molecular dynamics simulations to study the elastic properties and fracture patterns of transition metal dichalcogenide (TMD) MoX$_2$ (X = S, Se, Te) membranes, in their 2H and 1T phases, within the framework of the Stillinger–Weber potential. Results showed that the fracture mechanism of these membranes occurs through a fast crack propagation followed by their abrupt rupture into moieties. As a general trend, the translated arrangement of the chalcogen atoms in the 1T phase contributes to diminishing their structural stability when contrasted with the 2H one. Among the TMDs studied here, 2H-MoSe$_2$ has a higher tensile strength (25.98 GPa).

Keywords: transition metal dichalcogenides; molybdenum-based TMDs; elastic properties; fracture patterns; reactive molecular dynamics

1. Introduction

Transition metal dichalcogenide (TMD) monolayers are atomically thin semiconductors that belong to the family of 2*D* nanosheets [1,2]. They present an MX$_2$ arrangement, where M is a transition metal, and X is a chalcogen. The combination of chalcogen (e.g., S, Se, or Te) and transition metal atoms (typically Mo, W, Nb, Re, Ni, or V) yields more than 40 different materials [3,4]. Each monolayer has a thickness of 6–7 Å and is hexagonally-packed by transition metal atoms sandwiched between two layers of chalcogen atoms [3]. TMDs are graphene cognate and possible to be synthesized by applying the same chemical methods usually employed in producing the latter [5,6]. These materials have received much attention in the fields of biomedicine [7,8], optoelectronics [9,10], and energy conversion and storage [11,12]. Particularly, MoS$_2$ and MoTe$_2$ monolayers—direct bandgap semiconductors with bandgaps about 1.9 eV [13] and 1.0 eV [14], respectively—have emerged as promising candidates in replacing gapless graphene to develop novel applications in which semiconducting materials are desired [15]. MoSe$_2$, in turn, is an indirect bandgap semiconductor (with a bandgap about 1.58 eV [16]) that has also been widely employed in developing new applications in flat electronics [17,18]. To further explore the potential of these TMDs species in boosting new advances in the research fields mentioned above, their mechanical properties should be deeply understood.

TMD nanostructures have three different structural arrangements, named 2H, 1T, and 1T' [19]. 2H and 1T refer to the hexagonal and trigonal structures, respectively. The 1T' phase is a distorted form of 1T. The octahedral phase 1T can be spontaneously converted into its distorted octahedral phase 1T'. The 1T and 1T' phases have metallic and semiconducting characteristics, respectively [19,20]. Significant theoretical and experimental efforts have been employed in understanding the mechanical properties of layered MoS_2 [21–35], $MoSe_2$ [36–39], and $MoTe_2$ [14,40–45] on both 2H and 1T forms. In these investigations, they experimentally studied a few layers (5–25) of these TMDs species, and Young's modulus obtained ws approximately 330 GPa [22], 117 GPa [39], and 110 GPa [43] for MoS_2, $MoSe_2$, and $MoTe_2$, respectively. By using density functional theory and reactive molecular dynamic simulations, theoretical studies have predicted Young's modulus values for single-layer MoS_2, $MoSe_2$, and $MoTe_2$ ranging in the intervals 170–250 GPa [21,25,34], 165–185 GPa [39,46], and 60–115 GPa [42,44,45], respectively. These works promoted substantial advances in understanding the mechanical properties of TMDs. However, an overall description of their elastic properties and fracture dynamics is still missing.

Herein, we carried out extensive fully-atomistic reactive molecular dynamics simulations to study the elastic properties and fracture dynamics of MoX_2 (X = S, Se, Te) membranes in their 2H and 1T phases. The elastic properties were obtained from the stress–strain relationship. Only recently, 1T phases of these materials were experimentally realized [19]. In this sense, a detailed description of the mechanical properties of these nanostructures considering both 2H and 1T phases is highly attractive.

2. Details of Modeling

We performed fully-atomistic molecular dynamics (MD) simulations using the Stillinger–Weber (SW) [26,27] potential as implemented by LAMMPS [47]. Differently from regular MD simulations, in the reactive MD ones, the breaking and formation of bonds are described. Figure 1 illustrates the model TMD's monolayers studied here in their 2H and 1T phases. The left, middle, and bottom panels illustrate the MoS_2, $MoSe_2$, and $MoTe_2$ monolayers, respectively, in the H (top panels) and T phases (bottom panels). Their atomistic structure contains 3456, 3348, and 2688 atoms, respectively, and they were built intended in yielding 2D membranes with dimensions of about 100×100 Å^2, with periodic boundary conditions. It is worthwhile to stress that the simulation results are not sensitive to the selected computational cell size (as can occur when studying 2D materials using density functional theory calculations [48,49]), which has been checked using a system with larger dimensions. In this sense, the periodic boundary condition was applied to remove the lateral boundary effect and simulate the intrinsic properties of the MoX_2 membranes.

The equations of motion were solved using the velocity-Verlet integrator with a time-step of 0.1 fs. The tensile stress was considered in the system by applying a uniaxial strain along the periodic h and v directions, using an engineering strain rate of 10^{-6} fs^{-1}. The TMD membranes were stressed up to their complete rupture. To eliminate any residual stress within the membranes, they were equilibrated within an NPT ensemble at constant temperatures (1K and 300K) and null pressures using the Nosé–Hoover thermostat during 200 ps. By adopting this simulation protocol, Young's modulus (Y_M), fracture strain (FS), and ultimate strength (US) are the elastic properties derived from the stress–strain curves. The fracture dynamics, in turn, are studied through MD snapshots and the von Mises stress (VM) per-atom values, calculated at every 100 fs [50]. The VM values provide useful local structural information on the fracture mechanism, once they can determine the region from which the structure has started to yield the fractured lattice. The MD snapshots and trajectories were obtained by using free visualization and analysis software VMD [51].
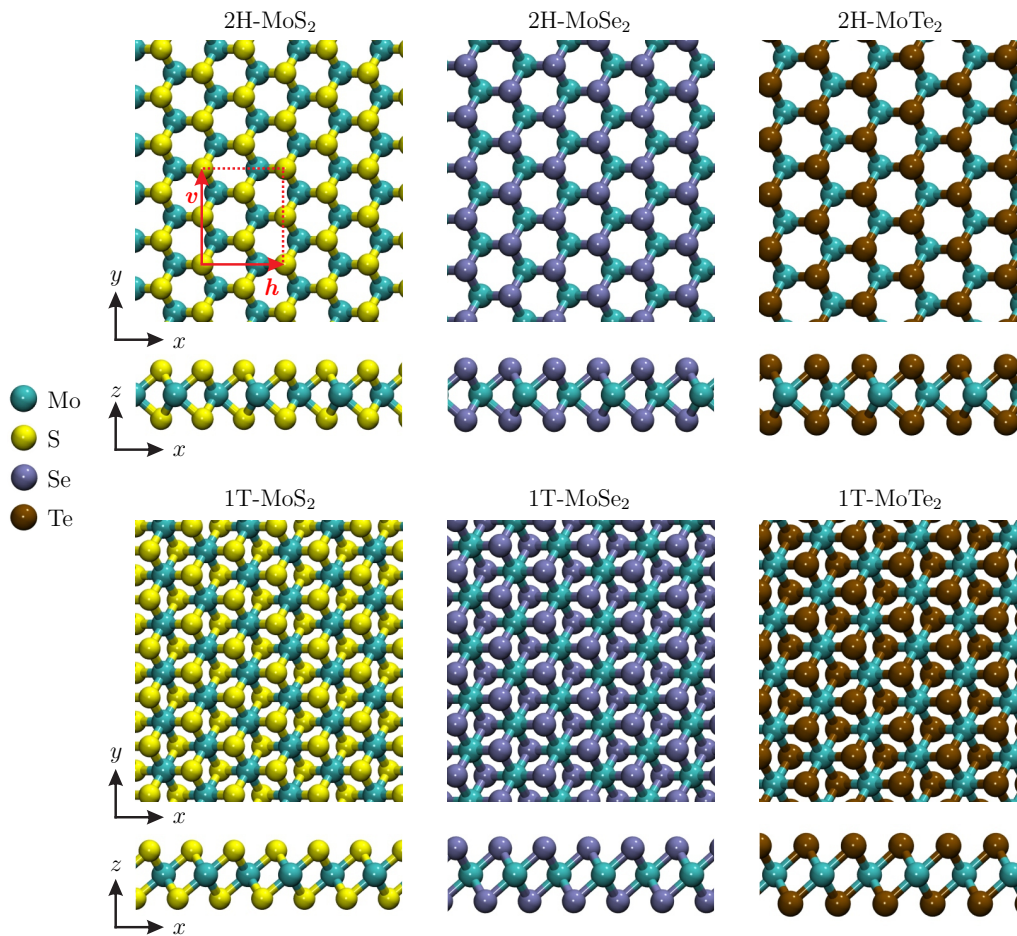
Figure 1. Schematic representation of the model transition metal dichalcogenide (TMD) monolayers in their 2H and 1T phases. The *v* and *h* red arrows highlighted in the 2H-MoS$_2$ panel denote the structure directions.

To better analyze the outcomes from the stretching dynamics, we calculated the von Mises stress (VM) per-atom values [52]. The VM values provide useful local structural information on the fracture mechanism, once they can determine the region from which the structure has started to yield the fractured lattice. In this way, the VM equation can be written as

$$\sigma_v^k = \sqrt{\frac{(\sigma_{xx}^k - \sigma_{yy}^k)^2 + (\sigma_{yy}^k - \sigma_{zz}^k)^2 + (\sigma_{xx}^k - \sigma_{zz}^k)^2 + 6((\sigma_{xy}^k)^2 + (\sigma_{yz}^k)^2 + (\sigma_{zx}^k)^2)}{2}}, \tag{1}$$

where σ_{xx}^k, σ_{yy}^k, and σ_{zz}^k are the components of the normal stress and σ_{xy}^k, σ_{yz}^k, and σ_{zx}^k are the components of the shear stress. The MD snapshots and trajectories were obtained by using free visualization and analysis software VMD [51].

In Equation (1), the elements of the per-atom stress tensor (computed by LAMMPS) are used. The tensor for each atom is symmetric with 6 components: *xx*, *yy*, *zz*, *xy*, *xz*, and *yz*. The computed quantity is in units of pressure*volume. It would need to be divided by a per-atom volume to have units of stress (pressure), but an individual atom's volume is not well defined or easy to compute in a deformed solid or a liquid. Therefore, if the diagonal components of the per-atom stress tensor are summed for all atoms in the system and the sum is divided by $D \times V$, where D is the dimension and V the volume of the system, respectively, the result should be $-P$, where P is the total pressure of the system [53–56].
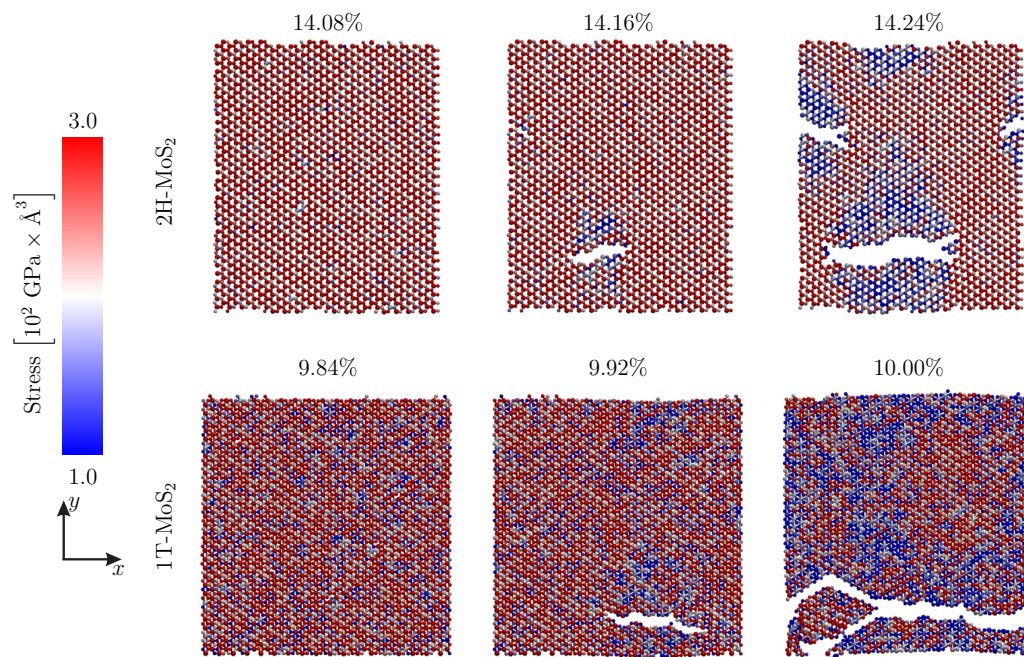
3. Results

We begin our discussions by showing representative MD snapshots of the fracture dynamics for the 2H-MoS$_2$ (top sequence of panels) and 1T-MoS$_2$ (bottom sequence of panels) monolayers at 300K and considering a uniaxial strain applied along the h-direction, as shown in Figure 2. In the 2H-MoS$_2$ case, one can note an abrupt rupture followed by a fast propagation of the fracture along the $v-$direction is accomplished at 11.60% of strain. The membrane is considered fractured at 11.68% of strain, once the atoms in the edges of the two fractures moieties are not interacting. A different fracture trend is realized for a 1T-MoS$_2$ membrane. The very first striking outcome obtained here, when contrasting the fracture dynamics of 2H-MoS$_2$ and 1T-MoS$_2$, is the considerably higher degree of fragility of the latter case. In Figure 2, one can observe that the critical strain for the beginning of the fracture in the 1T-MoS$_2$ (5.44%) is almost two times smaller than the one for 2H-MoS$_2$. Another clear trend showed in this figure is that the fracture dynamics of 1T-MoS$_2$ leads to a brittle lattice structure. This rupture trend is different from the one obtained for the 2H-MoS$_2$ case, in which two well concise MoS$_2$ fragments were produced as a final stage of the fracture process. This brittle signature for the 1T-MoS$_2$ case is obtained for 5.60% of strain. These results suggest that the translated arrangement of the chalcogen atoms in the 1T phase is crucial in diminishing the structural stability of TMDs.
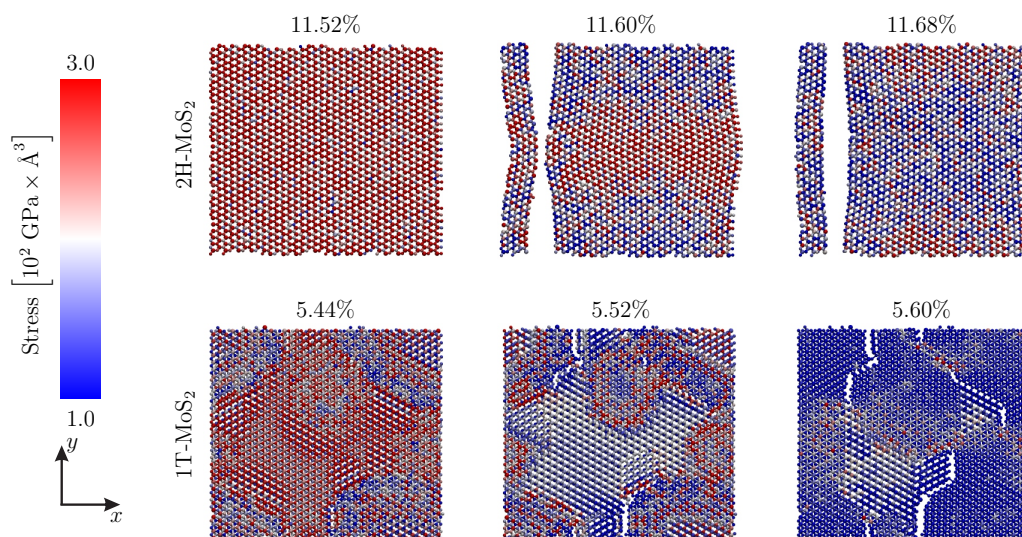
Figure 2. Representative molecular dynamics (MD) snapshots of the fracture dynamics for the 2H-MoS$_2$ (**top sequence of panels**) and 1T-MoS$_2$ (**bottom sequence of panels**) monolayers at 300K and considering a uniaxial strain applied along the h-direction.

An interesting result arises when a uniaxial strain is applied along the v-direction, as depicted in Figure 3. This figure shows the cases related to Figure 2. When the tensile stretching is applied in the v-direction, the critical strain to realize the beginning of the fracture of 2H-MoS$_2$ and 1T-MoS$_2$ membranes is considerably higher than the ones presented in Figure 2. The difference between the fracture strains for these species is smaller when the stretching is applied along the v-direction. As illustrated in Figure 3, the fracture (critical) strains for the beginning of the rupture are 14.08% and 9.84% for the 2H-MoS$_2$ and 1T-MoS$_2$ membranes, respectively. After that critical value, the crack propagation takes place for 14.16% and 9.92% for the 2H-MoS$_2$ and 1T-MoS$_2$ cases, respectively. Interestingly, the brittle trend for the 1T-MoS$_2$ fracture, obtained for the v-direction stretching, does not occur when it comes to the v-direction stretching. After 14.24% and 10.0%, a fast crack propagation occurs for the 2H-MoS$_2$ and 1T-MoS$_2$ monolayers, respectively.
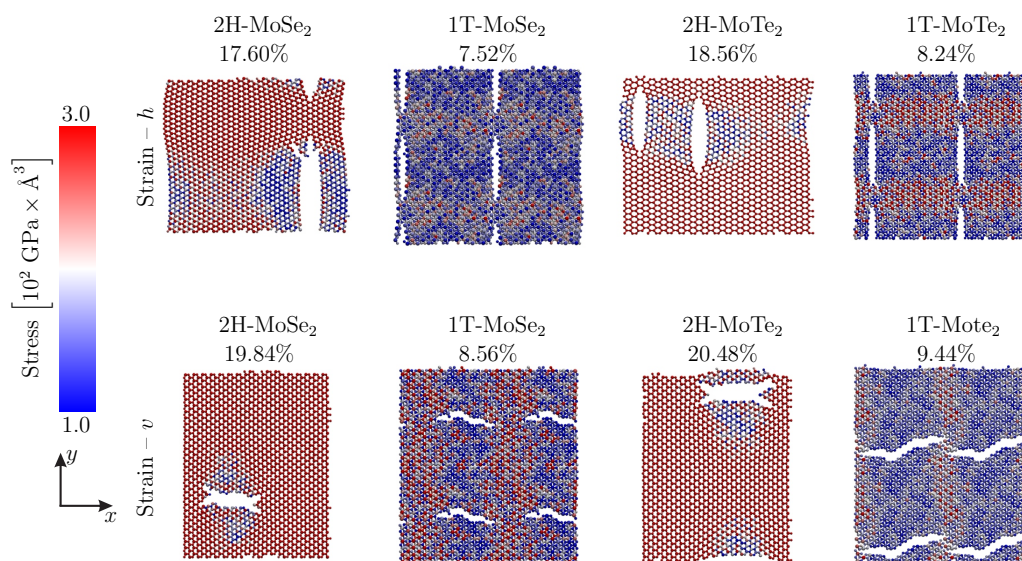
Figure 3. Representative MD snapshots of the fracture dynamics for the 1T-MoS$_2$ (**top sequence of panels**) and 1T-MoS$_2$ (**bottom sequence of panels**) monolayers at 300K and considering a uniaxial strain applied along the *v*-direction.

Figure 4 illustrates the representative MD snapshots for the 2H/1T-MoSe$_2$ and 2H/1T-MoTe$_2$ membranes. For the sake of convenience, we presented just the snapshots that show the crack propagation and the fractured form of these TMD species. The top and bottom panels depict the results when the uniaxial strain is applied along the *h* and *v* directions, respectively. In the top panels, one can note that the critical strain for the membrane rupture is 17.60%, 7.52%, 18.56%, and, 8.24% for the 2H-MoSe$_2$, 1T-MoSe$_2$, 2H-MoTe$_2$, and 1T-MoTe$_2$, respectively. In the bottom panels, we can observe that the critical strain for the membrane rupture is 19.84%, 8.56%, 20.48%, and, 9.44% for the 2H-MoSe$_2$, 1T-MoSe$_2$, 2H-MoTe$_2$, and 1T-MoTe$_2$, respectively. A comparison of the tensile strength among the TMDs studied here is presented below with Table 1. As for the MoS$_2$ cases, in the MoSe$_2$ and MoTe$_2$ cases, the fracture propagation undergoes in the direction opposite to the stretching. It is worthwhile to stress that both MoSe$_2$ and MoTe$_2$ present a fracture mechanism defined by a fast crack propagation followed by an abrupt rupture of the membranes into parts with a good degree of integrity (i.e., no brittle structures were observed). Theses results suggest that MoSe$_2$ and MoTe$_2$ monolayers may present greater structural stability than the MoS$_2$ ones.

Finally, we present the elastic properties obtained from the simulations discussed above. These properties are Young's modulus (Y_M, in units of GPa), fracture strain (FS (%)), and the maximum stress US (which is called ultimate tensile strength US (GPa)). They were estimated considering stretching regimes before mechanical failure (fracture) of the TMD membranes. These stretching regimes can be inferred from Figure 5, which illustrates the calculated stress–strain curves for all TMD membranes when subjected to 10K and 300K, considering a uniaxial strain applied in both *h* and *v* directions. Recently, the impact of temperature on the elastic properties of 2H-MoS$_2$ was studied by using the SW potential as implemented in LAMMPS [57]. The highest temperature simulated was 600K. It was concluded that Young's modulus decreased with increasing temperature. In addition, the 2H-MoS$_2$ has smaller fracture strain at a higher temperature. These behaviors were related to stronger thermal vibrations at higher temperatures, which resulted in longer extensions of atomic bonds. Figure 5a–f are describing the stress–strain relationship for the 2H/1T-MoS$_2$, 2H/1T-MoSe$_2$, and 2H/1T-MoTe$_2$ membranes, respectively. Table 1 presents a summary of the mechanical properties of the TMD monolayers studied in this work. In our simulation protocol, these monolayers were

stretched at a constant rate until their total rupture. The stress–strain curves show the two following common regions: a non-linear elastic region that is observed up to the ultimate strength value and a region of null stress (after a critical fracture strain) in which the TMD membranes ultimately break. In Figure 5, one can see that the US values are slightly higher for the cases in which the tensile stretching was applied in the v-direction. This trend occurs since the bond angle variations in $h-$ and $v-$direction are different, and they govern the fracture strain. The fracture strains range from 5.44% (1T-MoS$_2$ at 300K) up to 29.86% (2H-MoTe$_2$ at 10K). As expected, increasing the temperature to 300K, there is a decrease in the critical tensile strain (fracture strain) values for all TMD membranes (see Table 1). The highest Young's modulus was obtained for 2H-MoSe$_2$ monolayer at 10K (154.65 GPa). The TMD of the higher tensile strength (highest ultimate stress value) is the 2H-MoSe$_2$ membrane at 10K (25.98 GPa). As discussed above, generally, the translated arrangement of the chalcogen atoms in the 1T phase can contribute to diminishing their structural stability when compared with TMD membranes in the 2H phase. Importantly, Table 1 summarizes the elastic properties (Y_M, FS, and US) that were obtained by fitting the stress–strain curves for the TMD monolayers investigated here. It is worthwhile to stress that the fracture is a random process. The scatter for the elastic property values obtained using different MD trajectories is useful to estimate the precision of our calculations. In this way, we performed ten additional simulations for the 2H-MoS$_2$ case by changing the initial seed for the random number generation. In these simulations, the strain was applied in the h-direction at 300 K. We obtained the following values for the elastic properties: $Y_M = 135 \pm 13$ GPa, FS $= 12 \pm 2$%, and the US $= 14 \pm 3$ GPa.

Figure 4. Representative MD snapshots of the fracture dynamics for the 2H/1T-MoSe$_2$ and 2H/1T-MoTe$_2$ monolayers at 300K. The **top** and **bottom** sequence of panels refer to the simulations considering a uniaxial strain applied along the h and v directions, respectively.

Table 1. Elastic properties (Y_M, in units of GPa), fracture strain (FS (%)), and the maximum stress US (which is called ultimate tensile strength US (GPa)) that were obtained by fitting the stress–strain curves for the TMD monolayers investigated here.

| Temperature [K] | 2H-MoS$_2$ | | | | | |
| | Strain-*h* | | | Strain-*v* | | |
	Y_M [GPa]	FS [%]	US [GPa]	Y_M [GPa]	FS [%]	US [GPa]
10 K	145	19	19	139	22	17
300 K	135	12	14	130	14	14

| Temperature [K] | 2H-MoSe$_2$ | | | | | |
| | Strain-*h* | | | Strain-*v* | | |
	Y_M [GPa]	FS [%]	US [GPa]	Y_M [GPa]	FS [%]	US [GPa]
10 K	160	23	26	155	27	25
300 K	154	17	22	149	20	21

| Temperature [K] | 2H-MoTe$_2$ | | | | | |
| | Strain-*h* | | | Strain-*v* | | |
	Y_M [GPa]	FS [%]	US [GPa]	Y_M [GPa]	FS [%]	US [GPa]
10 K	125	25	23	122	30	21
300 K	121	18	19	118	20	18

| Temperature [K] | 1T-MoS$_2$ | | | | | |
| | Strain-*h* | | | Strain-*v* | | |
	Y_M [GPa]	FS [%]	US [GPa]	Y_M [GPa]	FS [%]	US [GPa]
10 K	124	13	12	120	14	11
300 K	133	5	7	110	8	8

| Temperature [K] | 1T-MoSe$_2$ | | | | | |
| | Strain-*h* | | | Strain-*v* | | |
	Y_M [GPa]	FS [%]	US [GPa]	Y_M [GPa]	FS [%]	US [GPa]
10 K	127	12	11	124	15	12
300 K	114	7	8	112	8	8

| Temperature [K] | 1T-MoTe$_2$ | | | | | |
| | Strain-*h* | | | Strain-*v* | | |
	Y_M [GPa]	FS [%]	US [GPa]	Y_M [GPa]	FS [%]	US [GPa]
10 K	118	13	11	114	16	11
300 K	107	8	8	103	9	8
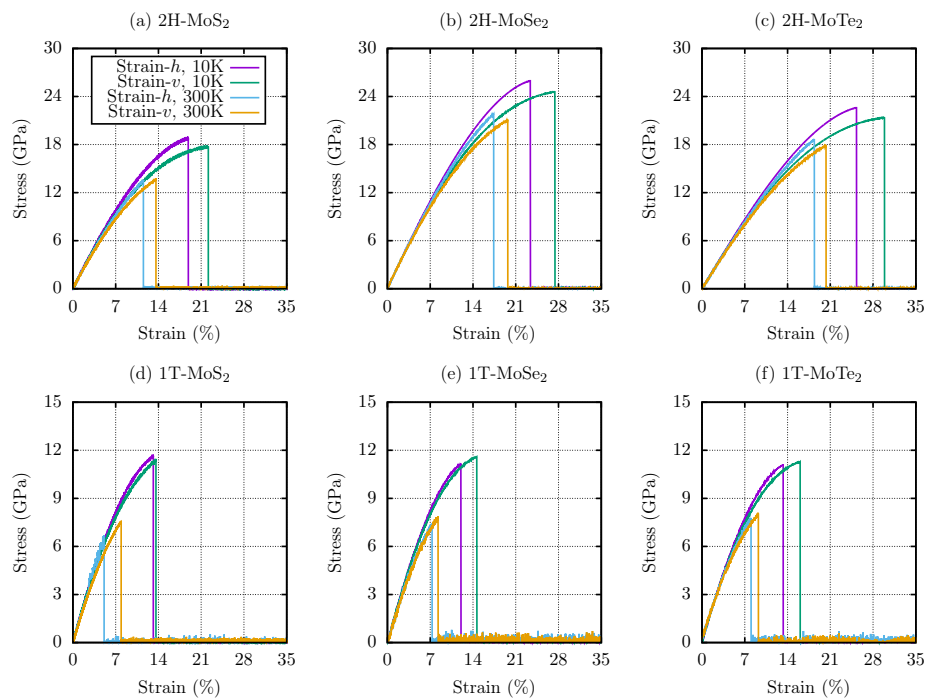
Figure 5. Calculated stress–strain curves for all TMD membranes studied here when subjected to 10K and 300K, considering a uniaxial strain applied in both *h* and *v* directions. (**a**,**d**), (**b**,**e**), and (**c**,**f**) are describing the stress–strain relationship for the 2H/1T-MoS$_2$, 2H/1T-MoSe$_2$, and 2H/1T-MoTe$_2$ membranes, respectively.

4. Discussion

In summary, we carried out fully-atomistic reactive molecular dynamics simulations to perform a comparative study on the elastic properties and fracture patterns of MoX$_2$ (X = S, Se, Te) membranes, in the 2H and 1T phases, within the framework of the Stillinger–Weber potential. The results showed that the fracture mechanism of a 2H-MoS$_2$ monolayer occurs through an abrupt rupture followed by fast crack propagation. A different fracture trend is realized for a 1T-MoS$_2$ membrane. The fracture dynamics of this material leads to a brittle structure. Both MoSe$_2$ and MoTe$_2$ presented a fracture mechanism defined by a fast crack propagation followed by an abrupt rupture of the membranes into parts with a good degree of integrity (i.e., no brittle structures were observed). These results suggest that these monolayers may present greater structural stability than the MoS$_2$ ones. The highest Young's modulus was obtained for 2H-MoSe$_2$ monolayer at 10K (154.65 GPa). The TMD of higher tensile strength is the 2H-MoSe$_2$ membrane at 300 K (21.88 GPa). Generally, the critical strain to realize the TMD membranes fracture is considerably higher when the strain was applied along the *v*-direction. It was also obtained here as a general trend that the translated arrangement of the chalcogen atoms in the 1T phase can contribute to diminishing their structural stability when compared with TMD membranes in the 2H phase. As a consequence, among the 2H and 1T phases, the 1T presented lower tensile strength. For instance, Young's modulus value for single-layer graphene is about 2.4 ± 0.4 TPa [58], which is almost ten times higher than the ones obtained here for the MoX$_2$ membranes. As it is well known, the lack of a bandgap in pristine graphene hampers its application in semiconducting devices. Since MoS$_2$ has a semiconducting bandgap (about 1.8 eV [22]) and possesses comparable tensile strength, it can be an alternative to substitute/complement graphene in semiconducting applications, mostly when it comes to the field of flat nano-electronics.

Author Contributions: M.L.P.J., J.M.D.S., C.M.V.d.A.: methodology, formal analysis, data Curation, and writing—original draft preparation. L.F.R.J., L.A.R.J., and R.T.d.S.J., and W.F.G.: conceptualization, supervision, funding acquisition, and writing—reviewing and editing. All authors have read and agreed to the published version of the manuscript.

Conflicts of Interest: The authors declare no conflict of interest.

References

1. Manzeli, S.; Ovchinnikov, D.; Pasquier, D.; Yazyev, O.V.; Kis, A. 2D transition metal dichalcogenides. *Nat. Rev. Mater.* **2017**, *2*, 17033. [CrossRef]

2. Chhowalla, M.; Shin, H.S.; Eda, G.; Li, L.J.; Loh, K.P.; Zhang, H. The chemistry of two-dimensional layered transition metal dichalcogenide nanosheets. *Nat. Chem.* **2013**, *5*, 263–275. [CrossRef]

3. Tan, C.; Zhang, H. Two-dimensional transition metal dichalcogenide nanosheet-based composites. *Chem. Soc. Rev.* **2015**, *44*, 2713–2731. [CrossRef]

4. Chhowalla, M.; Liu, Z.; Zhang, H. Two-dimensional transition metal dichalcogenide (TMD) nanosheets. *Chem. Soc. Rev.* **2015**, *44*, 2584–2586. [CrossRef]

5. Xu, M.; Liang, T.; Shi, M.; Chen, H. Graphene-like two-dimensional materials. *Chem. Rev.* **2013**, *113*, 3766–3798. [CrossRef] [PubMed]

6. Butler, S.Z.; Hollen, S.M.; Cao, L.; Cui, Y.; Gupta, J.A.; Gutiérrez, H.R.; Heinz, T.F.; Hong, S.S.; Huang, J.; Ismach, A.F.; et al. Progress, challenges, and opportunities in two-dimensional materials beyond graphene. *ACS Nano* **2013**, *7*, 2898–2926. [CrossRef] [PubMed]

7. Qian, X.; Shen, S.; Liu, T.; Cheng, L.; Liu, Z. Two-dimensional TiS 2 nanosheets for in vivo photoacoustic imaging and photothermal cancer therapy. *Nanoscale* **2015**, *7*, 6380–6387. [CrossRef] [PubMed]

8. Chen, Y.; Tan, C.; Zhang, H.; Wang, L. Two-dimensional graphene analogues for biomedical applications. *Chem. Soc. Rev.* **2015**, *44*, 2681–2701. [CrossRef]

9. Wang, Q.H.; Kalantar-Zadeh, K.; Kis, A.; Coleman, J.N.; Strano, M.S. Electronics and optoelectronics of two-dimensional transition metal dichalcogenides. *Nat. Nanotechnol.* **2012**, *7*, 699–712. [CrossRef]

10. Wilson, J.A.; Yoffe, A. The transition metal dichalcogenides discussion and interpretation of the observed optical, electrical and structural properties. *Adv. Phys.* **1969**, *18*, 193–335. [CrossRef]

11. Eda, G.; Yamaguchi, H.; Voiry, D.; Fujita, T.; Chen, M.; Chhowalla, M. Photoluminescence from chemically exfoliated MoS_2. *Nano Lett.* **2011**, *11*, 5111–5116. [CrossRef] [PubMed]

12. Yun, Q.; Lu, Q.; Zhang, X.; Tan, C.; Zhang, H. Three-dimensional architectures constructed from transition-metal dichalcogenide nanomaterials for electrochemical energy storage and conversion. *Angew. Chem. Int. Ed.* **2018**, *57*, 626–646. [CrossRef]

13. Mak, K.F.; Lee, C.; Hone, J.; Shan, J.; Heinz, T.F. Atomically thin MoS_2: A new direct-gap semiconductor. *Phys. Rev. Lett.* **2010**, *105*, 136805. [CrossRef] [PubMed]

14. Ruppert, C.; Aslan, O.B.; Heinz, T.F. Optical properties and band gap of single-and few-layer $MoTe_2$ crystals. *Nano Lett.* **2014**, *14*, 6231–6236. [CrossRef] [PubMed]

15. Jariwala, D.; Sangwan, V.K.; Lauhon, L.J.; Marks, T.J.; Hersam, M.C. Emerging device applications for semiconducting two-dimensional transition metal dichalcogenides. *ACS Nano* **2014**, *8*, 1102–1120. [CrossRef]

16. Zhang, Y.; Chang, T.R.; Zhou, B.; Cui, Y.T.; Yan, H.; Liu, Z.; Schmitt, F.; Lee, J.; Moore, R.; Chen, Y.; et al. Direct observation of the transition from indirect to direct bandgap in atomically thin epitaxial $MoSe_2$. *Nat. Nanotechnol.* **2014**, *9*, 111. [CrossRef]

17. Eftekhari, A. Molybdenum diselenide ($MoSe_2$) for energy storage, catalysis, and optoelectronics. *Appl. Mater. Today* **2017**, *8*, 1–17. [CrossRef]

18. Eda, G.; Maier, S.A. Two-dimensional crystals: Managing light for optoelectronics. *ACS Nano* **2013**, *7*, 5660–5665. [CrossRef]

19. Zhang, X.; Lai, Z.; Ma, Q.; Zhang, H. Novel structured transition metal dichalcogenide nanosheets. *Chem. Soc. Rev.* **2018**, *47*, 3301–3338. [CrossRef]

20. Yu, Y.; Nam, G.H.; He, Q.; Wu, X.J.; Zhang, K.; Yang, Z.; Chen, J.; Ma, Q.; Zhao, M.; Liu, Z.; et al. High phase-purity 1T'-MoS$_2$-and 1T'-MoSe$_2$-layered crystals. *Nat. Chem.* **2018**, *10*, 638–643. [CrossRef]

21. Ostadhossein, A.; Rahnamoun, A.; Wang, Y.; Zhao, P.; Zhang, S.; Crespi, V.H.; Van Duin, A.C. ReaxFF reactive force-field study of molybdenum disulfide (MoS$_2$). *J. Phys. Chem. Lett.* **2017**, *8*, 631–640. [CrossRef] [PubMed]

22. Castellanos-Gomez, A.; Poot, M.; Steele, G.A.; Van Der Zant, H.S.; Agraït, N.; Rubio-Bollinger, G. Elastic properties of freely suspended MoS$_2$ nanosheets. *Adv. Mater.* **2012**, *24*, 772–775. [CrossRef] [PubMed]

23. Castellanos-Gomez, A.; van Leeuwen, R.; Buscema, M.; van der Zant, H.S.; Steele, G.A.; Venstra, W.J. Single-layer MoS$_2$ mechanical resonators. *Adv. Mater.* **2013**, *25*, 6719–6723. [CrossRef] [PubMed]

24. Castellanos-Gomez, A.; Roldán, R.; Cappelluti, E.; Buscema, M.; Guinea, F.; van der Zant, H.S.; Steele, G.A. Local strain engineering in atomically thin MoS$_2$. *Nano Lett.* **2013**, *13*, 5361–5366. [CrossRef]

25. Cooper, R.C.; Lee, C.; Marianetti, C.A.; Wei, X.; Hone, J.; Kysar, J.W. Nonlinear elastic behavior of two-dimensional molybdenum disulfide. *Phys. Rev. B* **2013**, *87*, 035423. [CrossRef]

26. Jiang, J.W.; Park, H.S. Mechanical properties of MoS$_2$/graphene heterostructures. *Appl. Phys. Lett.* **2014**, *105*, 033108. [CrossRef]

27. Jiang, J.W.; Park, H.S.; Rabczuk, T. Molecular dynamics simulations of single-layer molybdenum disulphide (MoS$_2$): Stillinger-Weber parametrization, mechanical properties, and thermal conductivity. *J. Appl. Phys.* **2013**, *114*, 064307. [CrossRef]

28. Kang, J.; Sahin, H.; Peeters, F.M. Mechanical properties of monolayer sulphides: A comparative study between MoS$_2$, HfS 2 and TiS 3. *Phys. Chem. Chem. Phys.* **2015**, *17*, 27742–27749. [CrossRef]

29. Khan, M.B.; Jan, R.; Habib, A.; Khan, A.N. Evaluating mechanical properties of few layers MoS$_2$ nanosheets-polymer composites. *Adv. Mater. Sci. Eng.* **2017**, *2017*, 3176808. [CrossRef]

30. Liang, T.; Phillpot, S.R.; Sinnott, S.B. Parametrization of a reactive many-body potential for Mo–S systems. *Phys. Rev. B* **2009**, *79*, 245110. [CrossRef]

31. Liu, K.; Yan, Q.; Chen, M.; Fan, W.; Sun, Y.; Suh, J.; Fu, D.; Lee, S.; Zhou, J.; Tongay, S.; et al. Elastic properties of chemical-vapor-deposited monolayer MoS$_2$, WS$_2$, and their bilayer heterostructures. *Nano Lett.* **2014**, *14*, 5097–5103. [CrossRef] [PubMed]

32. Manzeli, S.; Allain, A.; Ghadimi, A.; Kis, A. Piezoresistivity and strain-induced band gap tuning in atomically thin MoS$_2$. *Nano Lett.* **2015**, *15*, 5330–5335. [CrossRef]

33. Yazyev, O.V.; Kis, A. MoS$_2$ and semiconductors in the flatland. *Mater. Today* **2015**, *18*, 20–30. [CrossRef]

34. Mortazavi, B.; Ostadhossein, A.; Rabczuk, T.; Van Duin, A.C. Mechanical response of all-MoS$_2$ single-layer heterostructures: A ReaxFF investigation. *Phys. Chem. Chem. Phys.* **2016**, *18*, 23695–23701. [CrossRef] [PubMed]

35. Miró, P.; Ghorbani-Asl, M.; Heine, T. Two dimensional materials beyond MoS$_2$: Noble-transition-metal dichalcogenides. *Angew. Chem. Int. Ed.* **2014**, *53*, 3015–3018. [CrossRef] [PubMed]

36. Frisenda, R.; Drüppel, M.; Schmidt, R.; de Vasconcellos, S.M.; de Lara, D.P.; Bratschitsch, R.; Rohlfing, M.; Castellanos-Gomez, A. Biaxial strain tuning of the optical properties of single-layer transition metal dichalcogenides. *NPJ 2D Mater. Appl.* **2017**, *1*, 1–7. [CrossRef]

37. Jaques, Y.M.; Manimunda, P.; Nakanishi, Y.; Susarla, S.; Woellner, C.F.; Bhowmick, S.; Asif, S.A.S.; Galvão, D.S.; Tiwary, C.S.; Ajayan, P.M.; et al. Differences in the Mechanical Properties of Monolayer and Multilayer WSe$_2$/MoSe$_2$. *MRS Adv.* **2018**, *3*, 373–378. [CrossRef]

38. Jiang, M.; Zhang, J.; Wu, M.; Jian, W.; Xue, H.; Ng, T.W.; Lee, C.S.; Xu, J. Synthesis of 1T-MoSe$_2$ ultrathin nanosheets with an expanded interlayer spacing of 1.17 nm for efficient hydrogen evolution reaction. *J. Mater. Chem. A* **2016**, *4*, 14949–14953. [CrossRef]

39. Iguiñiz, N.; Frisenda, R.; Bratschitsch, R.; Castellanos-Gomez, A. Revisiting the buckling metrology method to determine the Young's modulus of 2D materials. *Adv. Mater.* **2019**, *31*, 1807150. [CrossRef]

40. Johari, P.; Shenoy, V.B. Tuning the electronic properties of semiconducting transition metal dichalcogenides by applying mechanical strains. *ACS Nano* **2012**, *6*, 5449–5456. [CrossRef]

41. Kumar, A.; Ahluwalia, P. Mechanical strain dependent electronic and dielectric properties of two-dimensional honeycomb structures of MoX2 (X = S, Se, Te). *Phys. B Condens. Matter* **2013**, *419*, 66–75. [CrossRef]

42. Mortazavi, B.; Berdiyorov, G.R.; Makaremi, M.; Rabczuk, T. Mechanical responses of two-dimensional $MoTe_2$; pristine 2H, 1T and 1T' and 1T'/2H heterostructure. *Extrem. Mech. Lett.* **2018**, *20*, 65–72. [CrossRef]

43. May, P.; Khan, U.; Coleman, J.N. Reinforcement of metal with liquid-exfoliated inorganic nano-platelets. *Appl. Phys. Lett.* **2013**, *103*, 163106. [CrossRef]

44. Rano, B.R.; Syed, I.M.; Naqib, S. Ab initio approach to the elastic, electronic, and optical properties of $MoTe_2$ topological Weyl semimetal. *J. Alloys Compd.* **2020**, *829*, 154522. [CrossRef]

45. Sun, Y.; Pan, J.; Zhang, Z.; Zhang, K.; Liang, J.; Wang, W.; Yuan, Z.; Hao, Y.; Wang, B.; Wang, J.; et al. Elastic properties and fracture behaviors of biaxially deformed, polymorphic $MoTe_2$. *Nano Lett.* **2019**, *19*, 761–769. [CrossRef] [PubMed]

46. Deng, S.; Li, L.; Li, M. Stability of direct band gap under mechanical strains for monolayer MoS_2, $MoSe_2$, WS_2 and WSe_2. *Phys. E Low Dimens. Syst. Nanostruct.* **2018**, *101*, 44–49. [CrossRef]

47. Plimpton, S. Fast parallel algorithms for short-range molecular dynamics. *J. Comput. Phys.* **1995**, *117*, 1–19. [CrossRef]

48. Freitas, R.R.; de Brito Mota, F.; Rivelino, R.; De Castilho, C.; Kakanakova-Georgieva, A.; Gueorguiev, G.K. Tuning band inversion symmetry of buckled III-Bi sheets by halogenation. *Nanotechnology* **2016**, *27*, 055704. [CrossRef]

49. Dos Santos, R.; Rivelino, R.; de Brito Mota, F.; Gueorguiev, G.; Kakanakova-Georgieva, A. Dopant species with Al–Si and N–Si bonding in the MOCVD of AlN implementing trimethylaluminum, ammonia and silane. *J. Phys. D Appl. Phys.* **2015**, *48*, 295104. [CrossRef]

50. Pereira, M.L.; Ribeiro, L.A. Thermomechanical insight into the stability of nanoporous graphene membranes. *FlatChem* **2020**, *24*, 100196. [CrossRef]

51. Humphrey, W.; Dalke, A.; Schulten, K. VMD: Visual molecular dynamics. *J. Mol. Graph.* **1996**, *14*, 33–38. [CrossRef]

52. Mises, R.V. Mechanik der festen Körper in plastisch-deformablen Zustand. *Math. Phys. Klasse* **1913**, *4*, 582–592.

53. Heyes, D.M. Pressure tensor of partial-charge and point-dipole lattices with bulk and surface geometries. *Phys. Rev. B* **1994**, *49*, 755. [CrossRef] [PubMed]

54. Sirk, T.W.; Moore, S.; Brown, E.F. Characteristics of thermal conductivity in classical water models. *J. Chem. Phys.* **2013**, *138*, 064505. [CrossRef] [PubMed]

55. Thompson, A.P.; Plimpton, S.J.; Mattson, W. General formulation of pressure and stress tensor for arbitrary many-body interaction potentials under periodic boundary conditions. *J. Chem. Phys.* **2009**, *131*, 154107. [CrossRef]

56. Surblys, D.; Matsubara, H.; Kikugawa, G.; Ohara, T. Application of atomic stress to compute heat flux via molecular dynamics for systems with many-body interactions. *Phys. Rev. E* **2019**, *99*, 051301. [CrossRef]

57. Ghobadi, N. A comparative study of the mechanical properties of multilayer MoS_2 and graphene/MoS_2 heterostructure: Effects of temperature, number of layers and stacking order. *Curr. Appl. Phys.* **2017**, *17*, 1483–1493. [CrossRef]

58. Lee, J.U.; Yoon, D.; Cheong, H. Estimation of Young's modulus of graphene by Raman spectroscopy. *Nano Lett.* **2012**, *12*, 4444–4448. [CrossRef]